

See discussions, stats, and author profiles for this publication at: <https://www.researchgate.net/publication/231645194>

# Rovibrational Energy Transfer in Ne –Li<sub>2</sub>(A<sub>1</sub>Σ<sup>u</sup>+, v=0): Comparison of Experimental Data and Results from Classical and Quantum Calculations†

ARTICLE *in* THE JOURNAL OF PHYSICAL CHEMISTRY A · JUNE 2010

Impact Factor: 2.69 · DOI: 10.1021/jp103504a

---

CITATIONS

7

---

READS

20

4 AUTHORS, INCLUDING:



Brian Stewart

Wesleyan University

17 PUBLICATIONS 268 CITATIONS

SEE PROFILE

# Rovibrational Energy Transfer in Ne–Li<sub>2</sub>(A<sup>1</sup>Σ<sub>u</sub><sup>+</sup>, *v*=0): Comparison of Experimental Data and Results from Classical and Quantum Calculations<sup>†</sup>

Brian A. Stewart,<sup>\*,‡</sup> Troy N. Stephens,<sup>‡,⊥</sup> Barbara A. Lawrence,<sup>§</sup> and George C. McBane<sup>\*,||</sup>

Department of Physics, Wesleyan University, Middletown, Connecticut 06459, Department of Chemistry, Eastern Illinois University, Charleston, Illinois 61920, and Department of Chemistry, Grand Valley State University, Allendale, Michigan 49401

Received: April 19, 2010; Revised Manuscript Received: June 4, 2010

Absolute rate constants for rotational and rovibrational energy transfer in the system Ne–Li<sub>2</sub>(A<sup>1</sup>Σ<sub>u</sub><sup>+</sup>) were measured by a dispersed fluorescence technique following excitation of the (*v* = 0, *j* = 18) initial level of Li<sub>2</sub>(A<sup>1</sup>Σ<sub>u</sub><sup>+</sup>). The rate coefficients for Δ*v* = 0 processes decline monotonically with increasing |Δ*j*|. The Δ*v* = 1 rate coefficients are also peaked near Δ*j* = 0 but show a broad shoulder extending to approximately Δ*j* = 30. Classical trajectory calculations and accurate quantum mechanical close-coupled calculations were used to compute theoretical rate constants from an ab initio potential surface. The agreement between the classical and quantum calculations is very good. The calculations slightly overestimate the measured rate constants for Δ*v* = 0, Δ*j* ≤ 6 processes but underestimate those for Δ*v* = 0, Δ*j* ≥ 20, implying that the anisotropy of the ab initio surface is too small at short range and too large at long range. For Δ*v* = 1 collisions, the calculations agree well with experiment for Δ*j* ≤ 0 and show the correct qualitative behavior for positive Δ*j*, including both the peaking at Δ*j* = 0 and the shoulder extending to positive Δ*j*. However, they underestimate rate constants for Δ*v* = 1, Δ*j* > 0 collisions, disagreeing with experiment by a factor of 2 for Δ*j* ~ 20 but agreeing better at higher and lower Δ*j*. Analysis of classical trajectories indicates that the vibrationally inelastic collisions fall into two groups corresponding to equatorial and near-end impacts; the former generally produce small Δ*j* while the latter produce large Δ*j*. Studies of a simple model potential show that this dual mechanism may be a general phenomenon not limited to the particular potential surface employed here. Criteria controlling the relative importance of the two vibrational excitation routes are enumerated.

## 1. Introduction

The dominant qualitative model of atom–diatom vibrational energy transfer invokes a collinear approach of the atom and a resulting compressive force on the diatomic bond. In a recent review<sup>1</sup> focused on the influence of the seminal Landau–Teller model,<sup>2</sup> Nikitin and Troe trace this collinear treatment back to 1903 work of Jeans<sup>3</sup> and forward through a series of enhancements including SSH theory<sup>4</sup> to modern close-coupled calculations. The collinear model generally gives vibrational excitation and relaxation probabilities that are small, strongly dependent on collision energy, and roughly proportional to the initial quantum number of the diatom.

The collinear view of vibrational energy transfer has retained its role as the primary qualitative picture even as full-dimensional dynamical treatments have become computationally feasible. Nonetheless, many people have recognized that off-axis collisions or rotational motion can modify the vibrational transfer in significant ways. Vibrational excitation in three dimensions may differ through simple steric effects, through competition with rotational excitation for available energy, or through properties of the potential surface that make vibrational coupling stronger at configurations other than the linear one.

Schwartz and Herzfeld,<sup>5</sup> for example, used a “breathing sphere” isotropic model but suggested correcting it with a steric factor of 1/3 to account for orientation. Faubel and Toennies<sup>6</sup> studied a model that included a Morse diatomic oscillator and exponential repulsion between both atoms of the diatomic and the incoming perturber, finding that for most energies a C<sub>2*v*</sub> sideways approach was more effective in causing vibrational transitions than a collinear one. They were interested in backscattering experiments, so their study included only zero impact parameters, and rotational excitation was not considered. Shin<sup>7</sup> used a pairwise additive Lennard-Jones potential and an analytical model incorporating nonzero impact parameter to assess the importance of noncollinear collisions in vibrational excitation. Pritchard and coworkers have studied vibration-rotation competition through resonance effects.<sup>8–11</sup> McCaffery and coworkers have developed an “angular momentum model” and applied it to several processes including vibrational energy transfer.<sup>12</sup> In a study of state-to-state integral cross sections for H + CO scattering, Houston, Schatz, and coworkers<sup>13,14</sup> found that most vibrational excitation of the CO occurred during collisions that traversed the (bent geometry) HCO or COH wells, even though there was no complex formation. They concluded that the only energetically accessible regions where the interaction potential depended substantially on the CO bond length lay within those wells, so that only there could an adequate force be applied to the CO bond to cause vibrational excitation. Similarly, Zare and coworkers have recently reported level-to-level studies of rovibrational energy transfer in the H + D<sub>2</sub> system.<sup>15,16</sup> This system involves strong

<sup>†</sup> Part of the “Reinhard Schinke Festschrift”.

<sup>\*</sup> To whom correspondence should be addressed E-mail: B.A.S., bstewart@wesleyan.edu; G.C.M., mcbaneg@gvsu.edu.

<sup>‡</sup> Wesleyan University.

<sup>§</sup> Eastern Illinois University.

<sup>||</sup> Grand Valley State University.

<sup>⊥</sup> Current address: Apple, Inc., 1 Infinite Loop, MS 37-2FMW, Cupertino, CA 95014.

chemical interactions and includes the possibility of a reactive encounter. In the inelastic channel Zare and coworkers identified a vibrational excitation mechanism that depended on scattering from the outer (attractive) part of the interaction potential, and called it the “tug of war” mechanism.

Level-to-level atom-diatom rovibrational energy transfer experiments fall into several classes. The diatomic may be prepared by supersonic cooling into the ground rovibrational state, by photoexcitation into a specific level of an excited electronic state, or by overtone or double resonance techniques (notably stimulated emission pumping) into excited rovibrational levels of the ground electronic state. The collisions may occur in a thermal gas for measurements of rate coefficients, or in photolytic or crossed-beam arrangements for measurement of relative or absolute cross sections. Finally, the postcollision product may be detected by spontaneous fluorescence, by laser induced fluorescence, by resonant ionization, or by time-of-flight techniques. Examples of many of these combinations are cited in several reviews.<sup>17–20</sup>

The present paper describes dispersed laser induced fluorescence experiments that determine absolute level-to-level rate coefficients for rovibrational transitions in  $\text{Li}_2(\text{A}^1\Sigma_u^+)$  induced by Ne near 800 K. They fall therefore into the class using selective photoexcitation into an excited electronic state, thermal collisions, and dispersed fluorescence detection. The most heavily studied atom-diatom systems of this type include rare gases colliding with  $\text{I}_2(\text{B}^3\Pi_{0+u})$ <sup>21</sup> and with alkali dimers  $\text{Na}_2$ <sup>20,22</sup> and  $\text{Li}_2$ . The technique also has been applied extensively to polyatomic molecules.<sup>17</sup>

The  $\text{Li}_2(\text{A}^1\Sigma_u^+)$ -Ne system has a strongly anisotropic potential energy surface with a very shallow well.  $\text{Li}_2(\text{A}^1\Sigma_u^+)$  has a large rotational constant ( $B_e = 0.497 \text{ cm}^{-1}$ ) and a relatively low vibrational frequency ( $\omega_e = 255.47 \text{ cm}^{-1}$ ). Neon atoms can induce rovibrational transitions in  $\text{Li}_2$  with unusual efficiency. The dynamics of those transitions show several interesting features, including rotational rainbows, final rotational state distributions that depend strongly on  $\Delta v$ , and dynamical competition between rotational and vibrational excitation. We compare our measured rate coefficients to results computed from the potential surface of Alexander and Werner,<sup>23,24</sup> using both quasiclassical trajectory calculations and accurate quantum scattering calculations. We find that an unusual noncollinear excitation mechanism dominates the vibrational energy transfer, as suggested by Billeb and Stewart in 1995.<sup>25</sup> We argue from a potential model similar to that of Faubel and Toennies that the noncollinear mechanism is not peculiar to the particular potential surface being studied here.

## 2. Experiment

We use a fluorescence technique dating to the early 20th century experiments of Franck and Wood<sup>26</sup> that employs fluorescence intensity as a measure of collisionally populated excited-state levels. Experimental and analysis techniques very similar to those used here were described previously.<sup>11,27</sup>

The experimental concept is shown in Figure 1. The collisions under investigation occur in an electronically excited state. A single rovibrational level of the excited state is prepared using a continuous-wave single-frequency laser. The resulting fluorescence is dispersed and its spectrum recorded. The spectrum contains strong *parent lines* that emanate from laser-populated excited-state levels, and weaker *satellite lines* that emanate from collisionally populated excited-state levels. The intensities of the satellite lines depend upon the target gas pressure, and these intensities, after correction for line strength and instrument

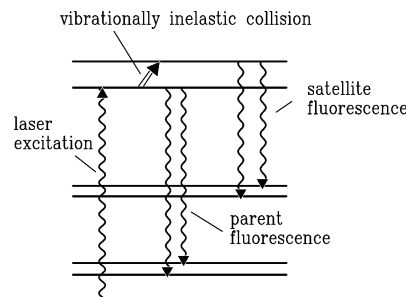


**Figure 1.** Experimental concept. Excitation from a single rovibrational level of the ground electronic state to a level in the A state is shown, along with fluorescence terminating on other levels of the ground state. Fluorescence originating from the laser-populated state is *parent* fluorescence, and fluorescence originating from collisionally populated excited-state levels is *satellite* fluorescence.

response, are proportional to the excited-state population densities. The steady-state rate equation

$$\frac{dn_f}{dt} = k_{if}n_i n_X - \Gamma_f n_f = 0 \quad (1)$$

solved for the ratio of satellite to parent population densities  $n_f/n_i$ , permits extraction of the level-to-level rate constant  $k_{if}$  from the pressure dependence on the rare gas pressure  $n_X$ . In practice, eq 1 is modified to correct for multiple collisions, as we discuss in the following section. The radiative decay rate  $\Gamma_f$  establishes single-collision conditions by limiting the time between excitation and radiative decay. It is known from previous measurements<sup>28</sup> and calculations.<sup>29</sup>

**2.1. Experimental Details.** The experimental apparatus used is shown in Figure 2. A four-arm stainless steel cell with Brewster windows contained lithium metal and neon gas. A flexible heater (ARI Industries) was wound around the cell and covered by two layers of heat shielding and 2.5 cm of refractory insulation. The center of the cell was maintained at a temperature of  $883 \pm 1 \text{ K}$  by means of a Eurotherm PID temperature controller. At this temperature, the vapor pressure of atomic lithium is 0.065 Torr, and the vapor pressure of the lithium dimer is  $9.5 \times 10^{-4} \text{ Torr}$ .<sup>30</sup> The neon pressure was varied from 0.76 to 5.3 Torr in four steps. Because the temperature of the cell was monitored by means of a type-K thermocouple welded to its surface, the temperature of the vapor at the center of the cell is uncertain by a few degrees.

A single-frequency Ti:sapphire laser (Coherent 899-29) pumped by a krypton-ion laser was used to prepare the  $v' = 0$ ,  $f' = 18$  level of  $\text{Li}_2(\text{A}^1\Sigma_u^+)$  by exciting the 0,0 P(19) transition at  $13\,936.1 \text{ cm}^{-1}$ .<sup>31</sup> A laser power stabilizer (Cambridge Research LPC) was used to maintain the laser power at 68 mW. A double monochromator (Spex 1404) was equipped with a photomultiplier tube (RCA C31034A) and photon counting electronics (SRS 400). The excellent stray light rejection of the double monochromator made it possible to accurately determine the intensities of the small spectral lines needed for this study. The monochromator was scanned from 11 600 to 12 300  $\text{cm}^{-1}$  in two segments. Before and after each segment was scanned, a short scan over a single parent line was made to ensure that the signal rate had not changed. Scan segments were discarded if a change of 5% or more in this parent line intensity occurred. The monochromator and its gratings are very sensitive to directional and polarization variations in the emitted radiation; for this reason, the polarization of the fluorescence was analyzed at  $54.7^\circ$  with respect to the polarization of the incident radiation

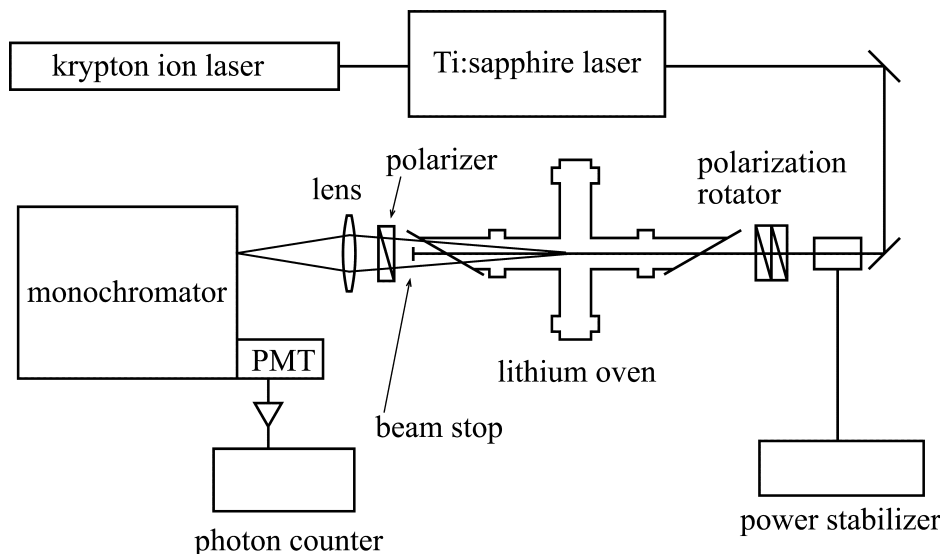


**Figure 2.** Experimental apparatus. Fluorescence from the laser-excited molecules is imaged onto the entrance slit of a double monochromator, and the spectrum is recorded by scanning the monochromator, using a photomultiplier tube and photon counting electronics. Polarization optics eliminate alignment effects and ensure best coupling of the fluorescence into the monochromator (see text).

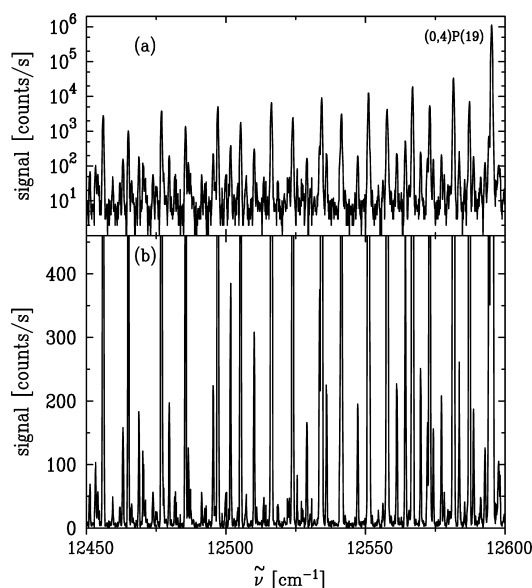


**Figure 3.** Section of the observed dispersed fluorescence spectrum. (a) The upper panel, on a semilog scale, shows one parent line (originating from the pumped *v* = 0, *j* = 18 level) and the satellite lines arising from collisional energy transfer. A strong progression of rotationally inelastic lines terminating on higher *j'* is visible. (b) The lower panel uses an expanded linear scale to depict more clearly the small inelastic lines corresponding to transitions with large  $\Delta j$  and with  $\Delta v > 0$ .

to eliminate alignment effects.<sup>32</sup> A portion of the experimental spectrum is shown in Figure 3.

**2.2. Data Analysis.** Details of the data analysis techniques we use have been given previously.<sup>11,27</sup> We summarize the method here, emphasizing modifications made since those earlier publications.

The parent line intensities measured before and after each scan were used to normalize the data for small changes in signal generation and collection, and a small correction was applied for pulse pileup (discriminator) error. The instrumental line shape was carefully determined by incrementing the monochromator in small steps over a parent line. The resulting data were fit by a piecewise continuous polynomial function; this fit was then used to fit the experimental lines at each pressure for the

purpose of extracting their intensities. The experimental spectrum is well known,<sup>31,33</sup> making semiautomatic assignment of the spectrum practical.

Line intensities determined in this manner were corrected for the instrument response and normalized by transition strength. The latter task was accomplished by dividing by the vibrational band strength, computed using the calculated X–A electronic transition moment,<sup>29,34</sup> and by the Hönl–London factor. Parent lines normalized in this way were then used to determine the instrument response function, giving us an internally consistent method for removing the spectral variation in the sensitivity of our detection system.

The line intensities normalized as described above are proportional to the excited-state population densities and may then be used to determine the rate constants from a rate model. For greater accuracy, we augment eq 1 to account for multiple collisions:

$$\frac{dn_f}{dt} = k_{if}n_i n_{\text{Ne}} + k_{if}^{\text{Li}}n_i n_{\text{Li}} - k_{Qf}n_f n_{\text{Ne}} - k_{Qf}^{\text{Li}}n_f n_{\text{Li}} - \Gamma_f n_f \quad (2)$$

Here  $k_Q$  and  $k_Q^{\text{Li}}$  represent depopulation of the final level *f* through inelastic and quenching collisions with the rare gas and atomic lithium, respectively. Solution of this equation in steady state yields the expression

$$\frac{n_f}{n_i} = \frac{k_{if}^{\text{Li}}n_{\text{Li}} + k_{if}n_{\text{Ne}}}{\Gamma_f + k_{Qf}^{\text{Li}}n_{\text{Li}} + k_{Qf}n_{\text{Ne}}} \quad (3)$$

Because the population densities appear only as a ratio on the left-hand side of eq 3, the constant of proportionality connecting the normalized line intensities with the excited-state population ratios drops out. In this way, absolute rate constants can be measured without the need for difficult measurements of absolute collection efficiency.

Least-squares fits of eq 3 to our pressure-dependent data yield the rate constants. The radiative lifetime  $1/\Gamma_f$  is about 19 ns over the range of molecular term energies in our experiment;

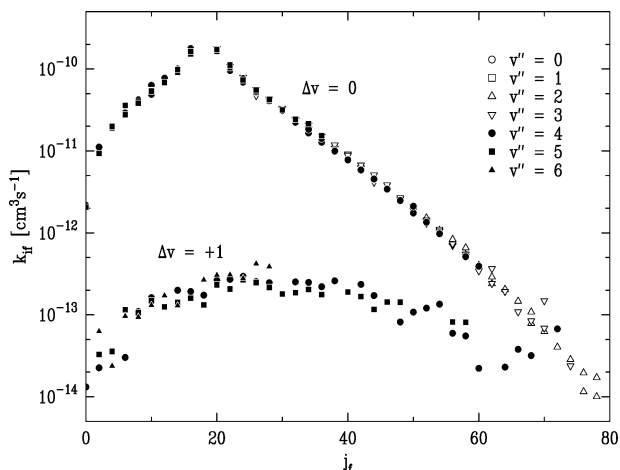


**Figure 4.** Observed level-to-level rate constants for  $\Delta v = 0$  and  $\Delta v = +1$ , shown on a semilogarithmic scale. Each plotted point results from the pressure dependence of a single observed satellite:parent line intensity ratio. The upper level is  $v' = 0$ , or 1,  $j' = 18$ , and the symbols given in the figure key indicate the  $v''$  levels to which the observed transition was made. Most final levels can be observed in more than one band and branch, so the spread among plotted points at a single final  $j$  indicates the experimental reproducibility.

we use the experimental lifetime data of Baumgartner et al.<sup>28,35</sup> in our analysis. The competing quenching cross sections are not well-known, however, and we neglect them in our analysis. Because  $k_{ij}^j n_{\text{Li}}$  is independent of  $n_{\text{Ne}}$  for a given final level, this term combines with  $\Gamma_f$  to produce an effective decay rate that is larger than the natural decay rate. The rate constants determined from eq 3 are thus lower bounds to the true rate constants. Using the quenching cross section  $\sigma_{\text{Li}}^j = 150 \pm 50 \text{ \AA}^2$  reported by Derouard and Sadeghi,<sup>36</sup> we estimate that the rate constants we report are low by less than 3% due to the neglect of this term.

Redundant determinations of the rate constants resulted from the multiple bands and branches on which each excited-state line could decay. Averaging these multiple measures improved the accuracy of the experimental rate constants. The individual measurements are shown in Figure 4; the spread in these measurements gives a good idea of the precision of the measurements. The resulting uncertainties, shown as explicit error bars in Figures 7 and 8, decline in general as the number of individual determinations increases, and the rovibrationally inelastic rate constants with particularly large error bars at  $j_f = 38, 50, 54$ , and 60 all arise from single determinations. The rovibrationally inelastic rate constant at  $j_f = 40$  also arises from a single measurement with a particularly good pressure fit, and its error bar was increased to more closely reflect the uncertainty attending unique measurements.

### 3. Calculations

**3.1. Potential Function.** Our classical and quantum mechanical calculations were carried out on the  $\text{Li}_2(\text{A}^1\Sigma_u^+)$ –Ne potential energy surface constructed by Alexander and Werner.<sup>23,24</sup> This potential function was obtained from multireference configuration interaction calculations carried out at the three  $\text{Li}_2$  internuclear separations 2.672, 3.108, and 3.493  $\text{\AA}$ ; the second of these values is the equilibrium internuclear separation. The inner and outer turning points of the diatomic molecular potential at  $v = 0$  are 2.926 and 3.314  $\text{\AA}$ ;<sup>32</sup> the three-body potential energy was obtained at these and other internuclear separations by interpolation, using a quadratic polynomial fit to the three calculated values.

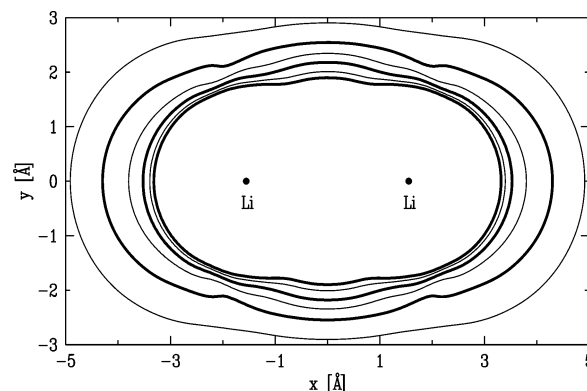


**Figure 5.** Equipotentials of the Alexander–Werner ab initio  $\text{Li}_2(\text{A}^1\Sigma_u^+)$  potential energy function with the diatom internuclear separation  $r$  fixed at its equilibrium value  $r_e = 3.108 \text{ \AA}$ . Heavy contours are at energies of 1000, 2000, and 3000  $\text{cm}^{-1}$  above the  $v = 0, j = 18$  reactant.

The Alexander–Werner potential has been used previously in quantum mechanical calculations of rotationally<sup>23,24</sup> and vibrationally<sup>23</sup> inelastic scattering, the latter in the coupled states<sup>37,38</sup> approximation. It has also been used by us in quasiclassical calculations in a number of studies of rotationally and vibrationally inelastic collisions.<sup>10,11,27,39</sup> The rotationally inelastic calculations agreed well with experimental thermally averaged rate constants<sup>27</sup> and speed-dependent cross sections.<sup>10</sup> Calculations of vibrational transfer at  $j_i = 30$  underestimated the rate constant at  $v_i = 2$  and overestimated it above  $v_i = 5$ .

Figure 5 shows equipotentials of the Alexander–Werner potential for its equilibrium Li–Li separation. The potential is very anisotropic: its expansion in Legendre polynomials includes terms through  $P_{18}(\cos \gamma)$ .<sup>24</sup> Similarly extreme potential anisotropy is present in the  $\text{Li}_2 \text{A}^1\Sigma_u^+$ –He system.<sup>40</sup> Most of the change in the potential due to the variation of  $r$  occurs at angles less than  $45^\circ$  from the molecular axis, implying that the strongest coupling to the molecular vibration occurs for collisions that are nearly collinear.

**3.2. Classical Calculations.** Classical trajectories on the Alexander–Werner potential surface were integrated using the fast action-angle approach of Smith.<sup>41</sup> This method assumes that  $\text{Li}_2(\text{A}^1\Sigma_u^+)$  is bound by a two-body potential of the form

$$U(r) = \frac{1}{2} \mu \omega^2 r_0^2 \left( \frac{r - r_0}{r} \right)^2 \quad (4)$$

where  $r$  is the molecular internuclear separation and  $r_0$  its equilibrium value,  $\mu$  is the reduced mass of the  $\text{Li}_2$  molecule, and  $\omega$  is its vibrational frequency. This simple potential function closely approximates the experimental molecular potential at low to moderate values of  $v$ .<sup>41</sup> The use of action-angle variables results in very efficient integration of the trajectories.

Trajectories were calculated at a total of 20 collision energies ranging from 15 to 3250  $\text{cm}^{-1}$ . At the lowest energies, which do not result in vibrational energy transfer, a total of 500 000 trajectories was sufficient to determine all but the smallest rotationally inelastic rate constants within a few percent. The vibrationally inelastic cross section becomes nonzero at a collision energy of 1300  $\text{cm}^{-1}$  but does not reach 0.01  $\text{\AA}^2$  until about 1700  $\text{cm}^{-1}$ . For this energy and the seven higher energies at which calculations were carried out, 5–25 million trajectories were needed to determine the small vibrationally inelastic cross sections to a few percent. At the highest collision energy, 3250  $\text{cm}^{-1}$ , a few of the 5 million trajectories reached a portion of



the Alexander–Werner potential for which the splines resulted in a physically inappropriate extrapolation of the ab initio points. These trajectories were discarded, and computation at higher energies was not included in our study. At this highest collision energy, the rotationally inelastic cross section contributes negligibly to the rate constant, but the vibrationally inelastic cross sections are still rising and require extrapolation as described in section 3.4.

Trajectories were binned using the standard histogram method,<sup>42,43</sup> using bins one unit wide in the vibrational action and two units wide in the rotational action, consistent with the symmetry constraint that requires even  $\Delta j$ . We experimented with reducing the bin width and rescaling as we did in an earlier study.<sup>11</sup> In the limit of vanishing bin width, this procedure would yield the classical result  $\sigma(j_i \rightarrow j_f) = d\sigma/dj$ . In the case of resonances such as the vibration–rotation resonances we observed earlier,<sup>11</sup> reducing the bin width sharpens the features, leading to better agreement with experiment. In the present case, the effect is to slightly reduce all cross sections. This reduction occurs because the density of final actions declines more rapidly than linearly across the bins with increasing  $|\Delta v|$  and  $|\Delta j|$ . The  $\Delta j = \pm 2$  cross sections for rotationally inelastic  $\Delta v = 0$  collisions were most strongly affected. The  $\Delta v = 1$  cross sections had increased thresholds which led to decreased rate constants. All our quasiclassical rate constants should therefore be regarded as upper bounds to the “true” classical rate constants.

**3.3. Quantum Calculations.** We carried out quantum scattering calculations on the Alexander and Werner potential energy surface with a parallel version<sup>44</sup> of the MOLSCAT program.<sup>45</sup> The calculations used Jacobi coordinates *R* for the distance between Ne and the Li<sub>2</sub> center of mass, *r* for the Li–Li distance, and  $\gamma$  for the angle between the corresponding vectors. For these calculations, radial strength functions  $V_{vjv'j'\lambda}(R)$  are required such that

$$\langle \phi_{vj}(r) | V(r, R, \gamma) | \phi_{vj'}(r) \rangle = \sum_{\lambda} V_{vjv'j'\lambda}(R) P_{\lambda}(\cos \gamma) \quad (5)$$

The  $\phi_{vj}(r)$  are vibrational wave functions of Li<sub>2</sub>(A<sup>1</sup>Σ<sub>u</sub><sup>+</sup>) in the internal state labeled by *v* and *j*,  $P_{\lambda}$  is a Legendre polynomial, and the angle brackets indicate integration over the diatomic bond length coordinate *r*. We obtained the radial strength functions from

$$V_{vjv'j'\lambda}(R) = \sum_{n=0}^2 v_n^{\lambda}(R) \langle \phi_{vj}(r) | (r - r_e)^n | \phi_{vj'}(r) \rangle \quad (6)$$

The  $v_n^{\lambda}(R)$  are defined in eq 11 of Alexander and Werner;<sup>24</sup> we used Alexander’s program to evaluate them. Our radial strength functions differ from theirs in two ways. First, we computed the functions  $\phi_{vj}(r)$  separately for each rotational level, rather than using a single  $\phi_v(r)$  for all rotational levels. We calculated the necessary moments  $\langle \phi_{vj}(r) | (r - r_e)^n | \phi_{vj'}(r) \rangle$  from the Li<sub>2</sub>(A<sup>1</sup>Σ<sub>u</sub><sup>+</sup>) potential curve of Lyyra and coworkers,<sup>47,48</sup> using the LEVEL program of Le Roy.<sup>48</sup> Second, Alexander and Werner used a quadratic expansion in  $(r - r_e)^n$  only for computing the off-diagonal ( $v \neq v'$ ) radial strength functions; for the diagonal functions, they used a linear expansion based on the two outermost values of *r* in the ab initio grid. Because we are interested in vibrational energy transfer at low *v*, we

used the quadratic expansion (their eq 11) for all the radial strength functions.

The calculations used the hybrid log derivative–Airy propagator of Alexander and Manolopolous.<sup>49,50</sup> We found, in agreement with Alexander and Werner, that the coupled states approximation was unreliable for this problem. We therefore performed accurate close coupled (CC) calculations up to a total energy of 3000 cm<sup>−1</sup>.

For each calculation, all the asymptotically open Li<sub>2</sub> levels were included in the basis set, as well as at least one closed rotational level for each *v*. With the propagator we used it is advantageous to perform calculations for several energies for each basis set, so calculations at lower energies often included many more closed levels. Between 1500 and 3000 cm<sup>−1</sup>, for example, the basis set included vibrational states up to *v* = 12, with maximum rotational levels of *j* = 82 in *v* = 0 and *j* = 20 in *v* = 12. The resulting basis sets included on the order of 4800 coupled channels. The energies of the Li<sub>2</sub>(A<sup>1</sup>Σ<sub>u</sub><sup>+</sup>) levels were computed from the molecular constants of Lyyra and coworkers.<sup>46,47</sup> The coupled channel equations were propagated out to at least 22 Å. At the highest energies it was necessary to include total angular momenta up to *J* = 250 to converge the partial wave expansion.

**3.4. Thermal Averaging.** The experimental rate constants reported above are not exactly ordinary thermal rate coefficients, because the distribution of collision speeds is modified from a normal thermal distribution by the Doppler selection of a particular velocity subgroup of parent molecules. For comparison with the experimental data, we calculated appropriate averaged quantities

$$k_{if}(T) = \int_0^{\infty} v P(v) \sigma_{if}(v) dv \quad (7)$$

where *P*(*v*) is the distribution of collision speeds *v* and  $\sigma_{if}(v)$  is the *v*-dependent inelastic cross section for the *i* → *f* transition. The speed distribution appropriate to our excitation of the initial state at line center is<sup>51</sup>

$$P(v) = \frac{v e^{-v^2/2(r+1)}}{\sqrt{r+1}} \operatorname{erf}\left(\frac{v}{\sqrt{2r(r+1)}}\right) \quad (8)$$

where  $r = m_{\text{Li}_2}/m_{\text{Ne}}$ , and the collision speed *v* is given in units of  $\sqrt{(kT/m_{\text{Li}_2})}$ .

The distribution of collision speeds *P*(*v*), though it is not a Maxwell distribution, can be closely approximated by one at a lower effective temperature *T*<sub>eff</sub>. For Li<sub>2</sub>–Ne, the experimental distribution slightly exceeds the effective Maxwell–Boltzmann distribution at low and high collision speeds and is slightly lower near its peak, which occurs at a slightly lower collision speed. The effective temperature can be determined from a formula given by Scott et al.;<sup>51</sup> we find *T*<sub>eff</sub> = 0.803 *T*<sub>cell</sub> = 709 K. These effective temperatures are useful for the purpose of comparing our experimental rate constants with true thermal rate constants. In constructing thermal rate constants from our calculated cross sections, however, we used eq 8.

We first generated a cubic spline passing through the computed  $\sigma_{if}(v)$  points, then used Simpson’s rule on a dense grid to evaluate the integral. For the pure rotational energy transfer processes, the integrand of eq 7 was already quite small at the highest *v* for which  $\sigma(v)$  was computed. For the vibrationally inelastic quantum cross sections, the integrand was decreasing at the highest available *v* but was not yet negligible,

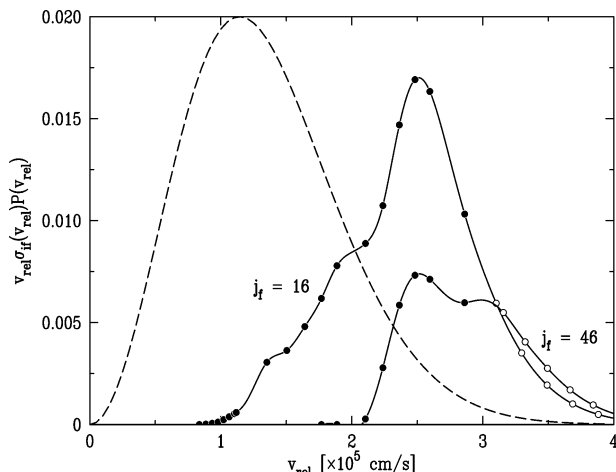


**Figure 6.** Integrand of eq 7 is shown as a function of collision speed for  $j_f = 16$  and  $j_f = 46$ . Filled symbols indicate results from the close-coupled quantum calculation on the ab initio potential surface; open symbols result from extrapolation of the cross sections by the method described in the text. The dashed line shows the experimental speed distribution given by eq 8 at the experimental temperature of 883 K.

so an extrapolation was required. The rovibrationally inelastic rate constants in  $\text{Li}_2(\text{A}^1\Sigma_u^+)$  obey an approximate  $(2j_f + 1)$  scaling law.<sup>52</sup> For the extrapolation we therefore scaled each of the computed  $\sigma_{if}(v)$  curves by  $(2j_f + 1)^{-1}$  and shifted it along the  $v$  axis by its threshold collision speed. This transformation produced a family of similar curves that varied over less than a factor of 2. We then extrapolated the curves to higher  $(v - v_{\text{thresh}})$ , using the directly computed curves for low  $\Delta j$  as guides for the extrapolation of the high  $\Delta j$  curves. The extrapolated curves were then shifted and scaled back to their original axes, interpolated using cubic splines, and used in eq 7 to produce rate constants. Examples of the extrapolated integrands are shown in Figure 6, along with the distribution of collision speeds given by eq 8 for our experimental temperature  $T = 883$  K. The  $(2j_f + 1)$  scaling is quite aggressive at large values of  $j_f$ , resulting in rate constants between  $j_f = 30$  and  $j_f = 50$  that are up to 25% larger than result from conservative manual extrapolations, and we consider the reported values in this range upper bounds to the true quantum rate constants.

The classical rovibrationally inelastic cross sections exhibited very different threshold behavior, with a sharp onset at a collision speed nearly independent of  $j_f$ . For this reason, we did not attempt a similar scaling for them. However, they extended to higher collision speed and were considerably less sensitive to extrapolation than the quantum cross sections.

#### 4. Comparison of Experiment and Computation

Experimentally determined rate constants for  $v_i = 0, j_i = 18$ , with  $\Delta v = 0$  and  $+1$  are given in Table 1 and shown in Figures 7 and 8. They are uncertainty-weighted averages of the data shown in Figure 4. We discuss the rotationally and rovibrationally inelastic results separately in the following subsections.

**4.1. Pure Rotational Energy Transfer.** The purely rotationally inelastic ( $\Delta v = 0$ ) rate constants are shown in Figure 7. The measured rate constants span more than 4 orders of magnitude. Rate constants from the quasiclassical and quantum mechanical calculations are also shown there.

There is very little difference between the two calculated sets of rate constants. However, both calculations are lower than experiment for large values of  $\Delta j$  and higher than experiment for small values of  $\Delta j$ , particularly for  $\Delta j = \pm 2$ . These trends

**TABLE 1: Experimental Rate Constants, in Units of  $10^{-11} \text{ cm}^3 \text{ s}^{-1}$  <sup>a</sup>**

$j_f$	$\Delta v = 0$	$\Delta v = 1$
0	0.2093(0.0190)	0.0013(0.0008)
2	0.9757(0.0700)	0.0028(0.0009)
4	1.9700(0.0544)	0.0031(0.0004)
6	3.2300(0.1187)	0.0100(0.0011)
8	3.8440(0.0481)	0.0108(0.0005)
10	5.2800(0.1993)	0.0133(0.0002)
12	6.8680(0.1167)	0.0125(0.0006)
14	9.7960(0.2318)	0.0165(0.0007)
16	16.3500(0.5576)	0.0164(0.0017)
18		0.0247(0.0013)
20	17.2300(0.7019)	0.0245(0.0010)
22	9.5760(0.0132)	0.0270(0.0011)
24	7.2750(0.3236)	0.0295(0.0003)
26	5.2380(0.1122)	0.0249(0.0008)
28	4.1750(0.0941)	0.0214(0.0009)
30	3.1660(0.0284)	0.0180(0.0019)
32	2.3860(0.0161)	0.0194(0.0015)
34	1.8480(0.0023)	0.0206(0.0005)
36	1.3000(0.0110)	0.0198(0.0013)
38	1.1210(0.0048)	0.0260(0.0029)
40	0.8057(0.0115)	0.0190(0.0003)
42	0.6188(0.0146)	0.0221(0.0016)
44	0.4388(0.0126)	0.0120(0.0011)
46	0.3546(0.0132)	0.0142(0.0012)
48	0.2540(0.0079)	0.0088(0.0016)
50	0.1813(0.0030)	0.0108(0.0034)
52	0.1409(0.0049)	0.0121(0.0005)
54	0.1074(0.0022)	0.0135(0.0021)
56	0.0751(0.0022)	0.0064(0.0006)
58	0.0655(0.0003)	0.0081(0.0000)
60	0.0395(0.0003)	0.0022(0.0043)
62	0.0276(0.0014)	0.0004(0.0001)
64	0.0193(0.0001)	
66	0.0122(0.0009)	0.0038(0.0013)
68	0.0108(0.0000)	0.0032(0.0014)
70	0.0063(0.0000)	
72	0.0047(0.0002)	
74	0.0028(0.0002)	
76	0.0012(0.0001)	
78	0.0016(0.0001)	
84	0.0005(0.0001)	

<sup>a</sup> The error bars, given in parentheses, are one standard deviation and include only statistical errors from the analysis.

are consistent with the close-coupled results of Alexander and Werner for  $v_i = 9, j_i = 22$ ,<sup>24</sup> except that their calculations did not extend to sufficiently high  $v_{\text{rel}}$  for them to construct rate constants above  $\Delta j = +4$ . The difference between experimental and computed rate constants may indicate that the ab initio potential surface is slightly too anisotropic at long range and insufficiently anisotropic at short range. Classical trajectories with impact parameters in the range 4–6 Å predominate in the  $\Delta j = \pm 2$  dynamics, while the  $\Delta j = 20$  rate constant results mostly from impact parameters 2–4 Å. These higher- $\Delta j$  collisions engage the repulsive core of the potential; if this shorter-range portion of the potential function is insufficiently anisotropic, insufficient torque will be generated and the result will be fewer high- $\Delta j$  collisions.

The energy-corrected sudden (ECS) scaling law,<sup>53</sup> combined with the exponential-power (EP) form for the basis rate constants,<sup>54</sup> has been employed previously with good success in modeling  $\text{Li}_2\text{--X}$  rate constants over a wide variety of initial levels.<sup>27,55</sup> An ECS-EP fit to the data is also shown in Figure 7.

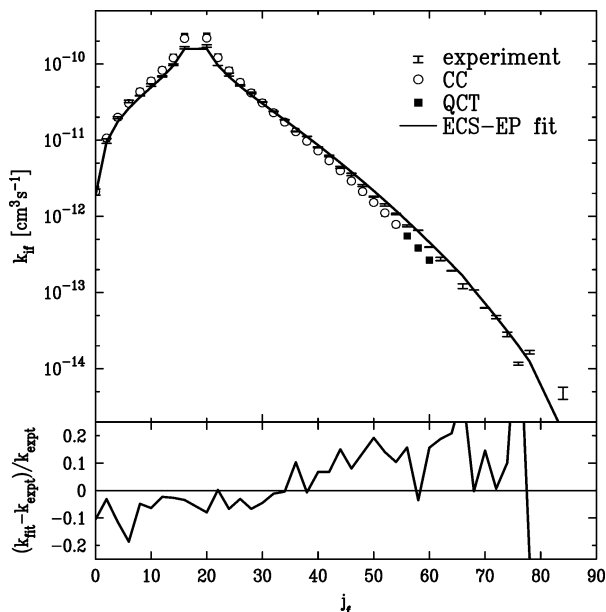


**Figure 7.** Rotationally inelastic rate constants. In addition to the experimental data, rate constants resulting from close-coupled (CC) and quasiclassical trajectory (QCT) calculations on the ab initio potential are shown. The CC and QCT results are very similar, with most of the latter being hidden beneath the CC results in the figure. The result of an ECS-EP fit to the data is shown as a line, and the residual from this fit is shown in the lower panel.

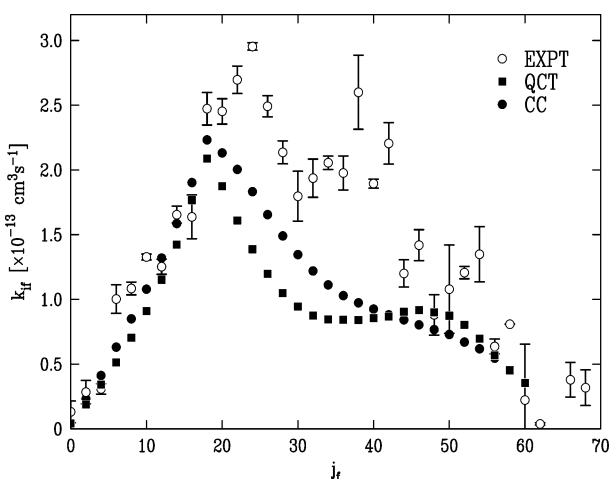


**Figure 8.** Experimental absolute rate constants for  $\Delta v = 1$  processes shown with the rate constants calculated from quasiclassical trajectories and from close coupled calculations on the ab initio potential surface. There are no adjustable parameters.

The ECS scaling law generates the matrix of rate constants  $\{k_{j_i \rightarrow j_f}\}$  from an array of basis rate constants  $\{k_{j \rightarrow 0}\}$  through the scaling relation

$$k_{j_i \rightarrow j_f} = (2j_f + 1)e^{-(E_{j_i} - E_{j_f})/kT} \sum_j (2j + 1) \begin{pmatrix} j & j_i & j_f \\ 0 & 0 & 0 \end{pmatrix}^2 A^2(j, j_{>}) k_{j \rightarrow 0} \quad (9)$$

where  $j_{>}$  is the larger of  $j_i$  and  $j_f$ ,  $E_{j_i}$  is the larger of  $E_i$  and  $E_f$ ,  $T$  is the temperature,  $\begin{pmatrix} j & j_i & j_f \\ 0 & 0 & 0 \end{pmatrix}$  is a 3- $j$  symbol, and  $A(j, j_{>})$  is an adiabatic factor given by

$$A(j, j_{>}) = \frac{1 + \tau_j^2/6}{1 + \tau_{j_{>}}^2/6} \quad (10)$$

This adiabatic factor constitutes the difference between ECS scaling and infinite-order sudden (IOS) scaling.<sup>56</sup> The scaled collision duration  $\tau_j = \omega_j T_d$ , with molecular rotational angular frequency  $\omega_j$  and collision duration  $T_d$ , is the number of radians through which the molecule rotates during a collision. This may be approximated as

$$\tau_j = 4\pi c B j l_c / \bar{v} \quad (11)$$

where  $c$  is the speed of light,  $B$  is the molecular rotational constant,  $l_c$  is a length characteristic of the atom–diatom interaction, and  $\bar{v}$  is the mean collision speed.

A complete fit to the data can be obtained by employing the exponential-power (EP) expression for the basis rate constants

$$k_{j \rightarrow 0} = a[j(j + 1)]^{-\gamma} e^{-(j/j^*)^2} \quad (12)$$

where  $a$ ,  $\gamma$ , and  $j^*$  are parameters determined from the fit. The parameter  $a$  is an overall scale factor; the exponent  $\gamma$  is determined by the  $R$ -dependence of the potential,<sup>57</sup> and  $j^*$  constitutes a measure of the long-range limit of the potential anisotropy, cutting off the rate constant distribution at large  $\Delta j$ .

The fit is quite good, exhibiting no profound variation from the data at any value of  $j_f$ ; the residual is shown beneath the data in Figure 7. The parameters obtained from the fit are given in Table 2, along with parameters from fits to the rate constants obtained from the close-coupled and quasiclassical calculations. The parameter  $l_c$  is not well determined in the fit to experimental data, but all parameters are accurately obtained from fits to the computed rate constants. The more rapid falloff at high  $j_f$  of the calculations on the ab initio potential surface results in a smaller value of  $j^*$ , limiting the values of  $j$  that can contribute to the rate constant in eq 9. This limitation has been interpreted as a reflection of angular momentum transfer limitations imposed by the finite anisotropy of the potential.<sup>58</sup> The ECS fits therefore support our argument that the potential surface is insufficiently anisotropic at short range.

**4.2. Rovibrational Energy Transfer.** The experimental rovibrationally inelastic rate constants are shown in Figure 8, along with rate constants from both quantum and quasiclassical calculations. We emphasize that there are no adjustable parameters. Our study is thus unusual (perhaps unique) in providing a three-way comparison among level-resolved experimental rate constants and both exact quantum and quasiclassical calculations on an ab initio potential surface and in making the comparison absolute.

Considering first the overall size of the rate constants, we note that experimental and calculated rate constants are small; the largest experimental value is approximately  $3 \times 10^{-13} \text{ cm}^3 \text{ s}^{-1}$ . The mean thermal collision speed  $\langle v \rangle$  at the effective temperature 709 K is  $1.35 \times 10^5 \text{ cm/s}$ . Division of the thermally averaged rate constants by this average collision speed results in cross sections no larger than  $0.02 \text{ \AA}^2$ . The calculated rate constants are even smaller than the experimental ones. Scaling of the quantum rate constants by the factor 1.35 and the classical rate constants by the factor 1.55 gives the least rms deviation from the experimental rate constants. In previous comparisons of measurements with classical calculations in this system,<sup>27,39</sup>



**TABLE 2: ECS-EP Parameters from Fits to Data (Expt) and Computation, Both Close-Coupled Quantum Calculations (CC) and Quasiclassical Trajectories (QCT)**

	$a$ (cm <sup>3</sup> s <sup>-1</sup> )	$l_c$ (cm)	$\gamma$	$j^*$
expt	$1.97(0.22) \times 10^{-10}$	$2.61(1.28) \times 10^{-8}$	0.778(0.010)	51.4(0.9)
CC	$3.63(0.07) \times 10^{-10}$	$3.03(0.08) \times 10^{-8}$	0.850(0.004)	41.8(0.3)
QCT	$4.01(0.01) \times 10^{-10}$	$3.01(0.10) \times 10^{-8}$	0.866(0.005)	42.3(0.3)

we found classical  $\Delta v = 1$  rate constants low by the factor 1.20 for  $v_i = 2$ ,  $j_i = 30$  results, but high for  $v_i \geq 5$ . The present results are in line with these previous observations in this respect. At the time, we conjectured that the disagreement might arise because of zero-point or threshold effects not included in the classical calculations.<sup>39</sup> Now, in view of the similarity in scale of the classical and quantum calculations, it seems more likely that the too-small size of the calculated rate constants at low  $v_i$  stems from a property of the ab initio potential surface.

A more detailed comparison of the experimental and computed rate constant distributions reveals that agreement is good from  $j_f = 0$  up to  $j_f = j_i$ , particularly with the quantum rate constants. At moderate positive values of  $\Delta j$ , however, a gap opens up between measurement and computation; this discrepancy becomes as large as a factor of 2 around  $j_f = 40$ , although scatter in the data makes it hard to quantify. The gap closes considerably at the highest measured  $j_f$  values.

The most important aspect of the agreement between experiment and computation is the peaking of all distributions near  $j_f = j_i$ . The peak appears clearly in the experimental results and both calculations. In addition, both the experiment and the quantum calculation show a long shoulder extending to large  $\Delta j$ , while the classical calculation shows a broad secondary maximum around  $\Delta j = 28$ . In the next section we seek a physical interpretation of this distribution.

**4.3. Origin of the Structures in the Cross Section and Rate Constant Distributions.** It is clear from the experimental results and the calculations that many vibrationally inelastic collisions transfer little angular momentum. Yet the near-collinear collisions that traditionally would be expected to be responsible for vibrational transfer are likely to generate large torques accompanying their large impulses along the internuclear axis. (True collinear collisions, of course, would not, but those are suppressed by a  $\sin \gamma$  weighting factor, and the potential anisotropy is so large that slightly off-axis collisions already have large moment arms.) We therefore turn to a more detailed analysis of the trajectory results.

The upper panel of Figure 9 shows calculated quasiclassical cross sections at a total energy of 2500 cm<sup>-1</sup>, corresponding to a collision energy of 2331.68 cm<sup>-1</sup>. We divide the cross sections into three groups according to the value of  $\Delta j$ : low (filled circles), intermediate (dots), and high (open squares). The distribution is clearly bimodal, dominated by a narrow peak at  $\Delta j = 0$ . The lower panel of Figure 9 shows the positions of closest approach for the same vibrationally inelastic trajectories. They are depicted against a backdrop of the equipotentials at the collision energy for representative values of  $r$ . The symbols match those used in the upper panel. The low- $\Delta j$  turning points are strongly clustered in a group near the equator of the molecule, while the high- $\Delta j$  impacts are distributed more diffusely nearer the end of the molecule.

The preponderance of equatorial impacts in the vibrationally inelastic trajectories is consistent with an unusual vibrational energy transfer mechanism described some time ago.<sup>25</sup> We describe this mechanism in detail as it applies to the present data in a separate publication;<sup>59</sup> here we outline its principal features and explore other aspects of the dynamics revealed by

the classical calculations and their comparison with the quantum calculations and with the experimental results.

Examination of the trajectories<sup>59</sup> indicates that during low- $j_i$  (equatorial) collisions the turning point is reached typically just before the *outer* extreme of the Li<sub>2</sub> vibrational motion, while high- $j_i$  (end-on) collisions turn predominantly just before the *inner* extreme. A direct consequence of the difference in the preferred phases of the equatorial and end-on impacts is that there is a region of the potential that generates no vibrational transfer. This is the separatrix (near  $\gamma = \pi/4$  for the ab initio potential) between bond-compressing end-on collisions and bond-stretching equatorial collisions. This dividing line is easily discerned in plots of  $\partial V/\partial r$ .<sup>25</sup> The relative contributions of these two groups of collisions, and hence the relative sizes of the low- $\Delta j$  and high- $\Delta j$  cross sections, are determined by three main factors: the location of the separatrix, which controls the fraction of trajectories encountering each region; the degree to which competition with pure rotational transfer suppresses vibrational transfer in the high- $\Delta j$  collisions; and the relative strengths of the vibrational coupling  $\partial V/\partial r$  in the two regions.

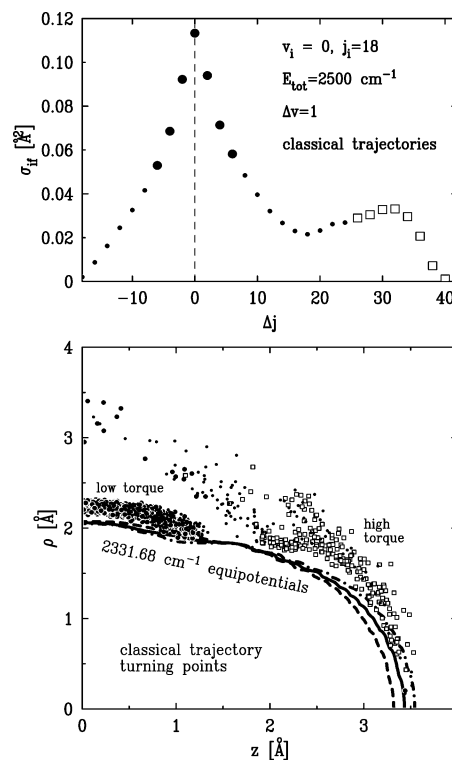


**Figure 9.** Upper panel: the quasiclassical rovibrationally inelastic cross section at a total energy  $E = 2500$  cm<sup>-1</sup>. Our partitioning of the final states into low, intermediate, and high  $\Delta j$  is shown by the different symbols. Lower panel: Positions of closest approach for individual trajectories producing  $\Delta v = 1$ . The  $\Delta j$  associated with each trajectory is indicated by its symbol as in the upper panel. The molecular equipotentials at the collision energy are also shown for three values of  $r$ : the inner classical turning point of the Li<sub>2</sub>(A<sup>1</sup>Σ<sub>u</sub><sup>+</sup>) vibrational motion, the equilibrium value, and the outer turning point. Due to molecular symmetry, only one-fourth of the equipotential needs to be shown; the end of the molecule lies in the lower right corner of the panel, while the molecular equator lies along the vertical axis.

Billeb and Stewart<sup>25</sup> provide a plot of  $\partial V/\partial r$ , showing that the translation–vibration coupling is substantial in accessible regions of the potential both near the end of the molecule and around the equator. It is larger around the ends. However, in the near-end regions, a substantial part of the collision energy may be transferred to rotation before the region of large  $\partial V/\partial r$  is reached. This loss of available energy into rotation reduces the vibrational energy transfer probability for near-end collisions. During equatorial impacts, the low-torque collisions produce little rotational excitation, so a larger fraction of the collision energy is available for vibrational excitation. The rate constants therefore peak at  $\Delta j = 0$  despite the smaller  $\partial V/\partial r$  in the equatorial region.

Rotational suppression of near-end vibrational transfer is probably limited to systems with a small molecular mass. Classically, the ratio of transferred rotational energy to the transferred angular momentum is  $j_i/2I$  when  $j_i = 0$ , so the disposal of energy into rotational energy is favored by small molecular moments of inertia. Systems with large moments of inertia will run out of angular momentum before the transferred rotational energy is very large,<sup>58</sup> limiting the competition of rotational excitation with vibrational excitation.

Another potential explanation considers the steepness of the repulsive wall of the potential in the equatorial and polar regions. The local steepness of the potential varies with the Jacobi angle  $\gamma$ . Although the ab initio potential surface does not decline exactly exponentially with increasing  $R$ , it is fit well by an exponential function  $V(R) \sim V_0 e^{-\alpha R}$  over a limited range of energies. For the high energies that lead to vibrational excitation, we find  $\alpha \approx 0.9 \text{ \AA}^{-1}$  for  $\gamma = 0$  (end-on impacts) and  $\alpha \approx 0.6 \text{ \AA}^{-1}$  for  $\gamma = \pi/2$  (equatorial impacts); that is, the molecule is a little harder on the ends. If we then approximate the typical interaction length as  $a = 2/\alpha$ , these values may be used to calculate the Massey adiabatic parameter  $\xi$ .<sup>60</sup> Energy transfer is expected to be efficient when this parameter is near unity and to decline exponentially for  $\xi > 1$ . The Massey parameter may be determined from  $\xi = a\Delta E/h\langle v \rangle$ , where  $\Delta E$  is the vibrational excitation energy. We find  $\xi \approx 1.2$  for  $\gamma = 0$  and  $\xi \approx 2.0$  for  $\gamma = \pi/2$ . Simple considerations of adiabaticity therefore predict that end-on collisions should be slightly more efficient than equatorial collisions for vibrational transfer on the Alexander–Werner potential surface and cannot explain the peaking at  $\Delta j = 0$  we observe.

It is natural to ask whether this dominance of equatorial impacts for vibrational excitation is general or depends on some quirk of the ab initio potential. To explore its generality, we constructed a very simple pairwise-additive exponentially repulsive (“Born–Mayer”<sup>61</sup>) potential of the form

$$V(r, R, \cos \gamma) = V_0(e^{-\alpha r_{AC}} + e^{-\alpha r_{BC}}) \quad (13)$$

where  $r_{AC}$  and  $r_{BC}$  are the distances from the centers of the two lithium atoms A and B to the Ne atom C. There are only two adjustable parameters,  $V_0$  and  $\alpha$ ;  $V_0$  simply controls the overall size of the potential, and  $\alpha$  determines the steepness of the exponential repulsion. To represent the diatomic, we added a simple harmonic oscillator potential in  $r_{AB}$  with equilibrium internuclear separation  $r_e = 3.108 \text{ \AA}$  and vibrational spectroscopic constant  $\omega_e = 255 \text{ cm}^{-1}$ .<sup>31</sup> The anisotropy of the molecule is determined by the equilibrium internuclear separation  $r_e$  and the steepness parameter  $\alpha$  through the two-body potential and is not an independently adjustable parameter. This model is very similar to that used by Faubel and Toennies.<sup>6</sup> The two constants

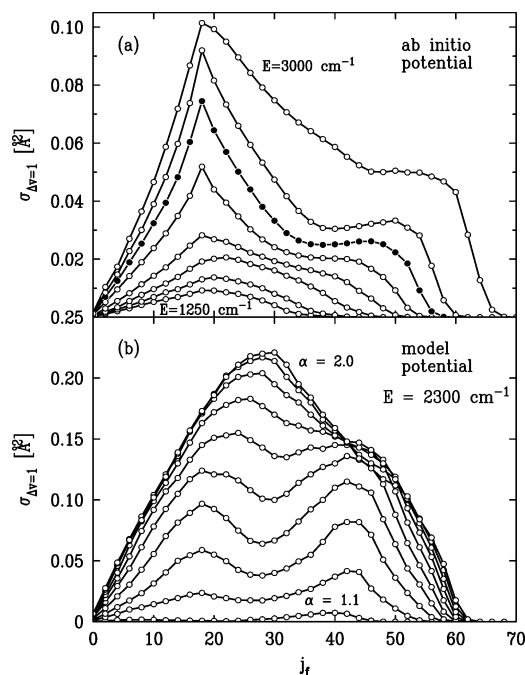


**Figure 10.** (a) Rovibrationally inelastic cross sections from close-coupled quantum calculations are shown at the following total energies (in  $\text{cm}^{-1}$ ): 1250, 1400, 1700, 1900, 2100, 2300, 2500, and 3000. The bimodal structure develops at intermediate collision energies and begins to be filled in at the highest collision energy. Filled circles denote collisions at  $E = 2300 \text{ cm}^{-1}$ , the energy at which the model calculations shown in the lower panel were calculated. (b) Dependence of the rovibrationally inelastic cross section on the exponential parameter  $\alpha = 1/L$ . The calculations were carried out at total energy of  $2300 \text{ cm}^{-1}$ .

$V_0$  ( $2000 \text{ cm}^{-1}$ ) and  $\alpha$  ( $1.5 \text{ \AA}^{-1}$ ) were adjusted by hand to give the best overall agreement with the vibrationally inelastic experimental results.

The results of a trajectory calculation using the model potential are qualitatively similar to those shown in Figure 9. The bimodal distribution is clearly present in the model calculation, demonstrating that a complex and particular form of the three-body potential is not required to generate the bimodal distribution. The most significant difference is in the relative importances of the low- $\Delta j$  and high- $\Delta j$  groups of collisions. The less-anisotropic model potential has a smaller band of equatorial impacts and a correspondingly larger band of end-on impacts, with the separatrix nearer to  $\gamma = 60^\circ$  than the value of  $45^\circ$  for the ab initio potential.

We thus see that the phenomenon of separate groups of impacts dividing the vibrationally inelastic rate constants into two groups and resulting in a bimodal  $j_f$  distribution is not specific to the Alexander–Werner potential and might indeed be a quite general dynamical phenomenon. The question remains as to why the experimental data do not show clear bimodal behavior. To address this question, we first examine the energy dependence of the rovibrationally inelastic cross section and show that increased collision energy fills in the gap between the two peaks. We then demonstrate that the energy at which the peaks merge is very sensitive to the stiffness of the three-body potential.

The upper panel of Figure 10 shows the energy dependence of the vibrationally inelastic cross section distributions from the quantum calculation on the ab initio potential surface. At the lowest collision energies, insufficient energy is available to populate many levels with positive  $\Delta j$ . As the collision energy

risks, the bimodal structure shown in Figure 9 develops. Then, at the highest calculated energy of  $3000\text{ cm}^{-1}$ , the intermediate values of  $\Delta j$  fill in. We observe the same behavior in the classical calculations on both the ab initio and model potential surfaces.

As the collision energy rises, a greater range of  $\Delta j$  values becomes accessible, because of both increased available energy and available orbital angular momentum. The collisions also become shorter in duration. The shortening effect can be brought about in another way: by making the potential “harder”, i.e., decreasing its range by making  $\alpha$  in eq 13 larger. In the lower panel of Figure 10, we show the effect of varying this parameter in the model potential. The result is similar to that brought about by increasing the energy. This comparison leads us to a hypothesis concerning the disagreement between the experimental and calculated rate constants in the intermediate  $\Delta j$  range: it is possible that the ab initio potential is too “soft”, i.e., varies too slowly with  $R$  throughout some significant portion of its range.

## 5. Conclusion

This study of inelastic scattering in  $\text{Li}_2(\text{A}^1\Sigma_u^+)-\text{Ne}$  is the first to our knowledge that compares absolute level-resolved rovibrationally inelastic rate constants with exact quantum and classical calculations on an ab initio potential surface. It has resulted in a number of observations. Pure rotationally inelastic scattering is reasonably well modeled by both classical and quantum mechanical calculations on the ab initio potential energy surface of Alexander and Werner. The discrepancies—the calculated rate constants are too high at low  $\Delta j$  and too low at high  $\Delta j$ —are consistent with a potential function whose anisotropy is too large at long range but too small at short range. The ECS-EP model, with its four adjustable parameters, is able to summarize the data to within 10% over the 4 orders of magnitude spanned by the observed rate constants.

The calculated rovibrationally inelastic rate constants agree with their observed counterparts for  $\Delta j \leq 0$  essentially quantitatively. For positive  $\Delta j$ , experimental rate constants exceed calculated ones; at  $j_f \approx 40$ , the measured rate constants are roughly double the rate constants from the quantum calculation. The experimental rate constant distribution is consistent with a mechanism that involves vibrational excitation via distinct groups of impacts that are either equatorial or near-end. The equatorial impacts produce little rotational excitation and contribute principally to the rate constants centered around  $\Delta j = 0$ , while the near-end impacts contribute to rate constants with large  $\Delta j$ . Classical calculations on a simple Born–Mayer potential function reproduce this behavior and also suggest that the computed rate coefficient distributions may not match the observed one because the potential is slightly too soft.

The factors that determine the relative importance of the two groups of vibrationally inelastic collisions include the relative coupling strength  $\partial V/\partial r$  in accessible regions of the potential, the location of the separatrix between the two regions of vibrational coupling, and the extent of rotation/vibration competition. The competition is in turn affected by the potential anisotropy, the steepness of the repulsive wall, and the kinematics; highly anisotropic systems with light atoms are likely to show stronger suppression of vibrational excitation.

We previously speculated<sup>39</sup> that discrepancies between experimental and classically calculated rate constants might be due to shortcomings of classical mechanics such as its failure to sequester the zero point energy. However, the agreement in overall size and shape of the classical and quantum rate constant distributions implicates the potential function in the present case.

The Alexander–Werner ab initio potential surface was published in 1991. It has proven very useful in comparisons of experimental and calculated rate constants. However, it was calculated for only three internuclear separations and a limited range of energies; moreover, the state of the art in excited-state molecular ab initio calculations has advanced since that time. Peterson<sup>62</sup> has calculated a new version of this potential surface, and we are carrying out calculations to see whether it addresses the shortcomings of the earlier surface outlined here.

**Acknowledgment.** We are grateful to Professor William Stwalley for the use of his laser laboratory at the University of Connecticut, and we thank Kristin Burgess and Kolo Wamba for their assistance with data acquisition. We thank Wesleyan University for computer time supported by the NSF under grant number CNS-0619508 and also acknowledge support from the San Diego Supercomputing Center for computations carried out there. Acknowledgement is made to the Donors of The Petroleum Research Fund, administered by the American Chemical Society, for the support of this research.

## References and Notes

- (1) Nikitin, E. E.; Troe, J. *Phys. Chem. Chem. Phys.* **2008**, *10*, 1483–1501.
- (2) Landau, L.; Teller, E. *Phys. Z. Sow.* **1936**, *10*, 34.
- (3) Jeans, J. H. *Philos. Mag.* **1903**, *6*, 279.
- (4) Schwartz, R. N.; Slawsky, Z. I.; Herzfeld, K. F. *J. Chem. Phys.* **1952**, *20*, 1591–1599.
- (5) Schwartz, R. N.; Herzfeld, K. F. *J. Chem. Phys.* **1954**, *22*, 767–773.
- (6) Faubel, M.; Toennies, J. P. *Chem. Phys.* **1974**, *4*, 36–44.
- (7) Shin, H. K. *Chem. Phys. Lett.* **1970**, *7*, 436–438.
- (8) Stewart, B.; Magill, P. D.; Scott, T. P.; Derouard, J.; Pritchard, D. E. *Phys. Rev. Lett.* **1988**, *60*, 282–285.
- (9) Magill, P. D.; Stewart, B.; Smith, N.; Pritchard, D. E. *Phys. Rev. Lett.* **1988**, *60*, 1943–1946.
- (10) Scott, T. P.; Smith, N.; Magill, P. D.; Pritchard, D. E.; Stewart, B. *J. Phys. Chem.* **1996**, *100*, 7981–7988.
- (11) Stewart, B.; Magill, P. D.; Pritchard, D. E. *J. Phys. Chem. A* **2000**, *104*, 10565–10575.
- (12) McCaffery, A. J.; Marsh, R. J. *J. Phys. Chem. A* **2000**, *104*, 10442–10451.
- (13) Chawla, G. K.; McBane, G. C.; Houston, P. L.; Schatz, G. C. *J. Chem. Phys.* **1988**, *88*, 5481–5488.
- (14) McBane, G. C.; Kable, S. H.; Houston, P. L.; Schatz, G. C. *J. Chem. Phys.* **1991**, *94*, 1141–1149.
- (15) Goldberg, N. T.; Zhang, J.; Koszinowski, K.; Bouakline, F.; Althorpe, S. C.; Zare, R. N. *Proc. Natl. Acad. Sci.* **2008**, *105*, 18194–18199.
- (16) Greaves, S. J.; Wrede, E.; Goldberg, N. T.; Zhang, J.; Miller, D. J.; Zare, R. N. *Nature* **2008**, *454*, 88–91.
- (17) Flynn, G. W.; Parmenter, C. S.; Wodtke, A. M. *J. Phys. Chem.* **1996**, *100*, 12817–12838.
- (18) Krajnovich, D. J.; Parmenter, C. S.; Catlett, D. L. *Chem. Rev.* **1987**, *87*, 237–288.
- (19) Silva, M.; Jongma, R.; Field, R. W.; Wodtke, A. M. *Annu. Rev. Phys. Chem.* **2001**, *52*, 811–852.
- (20) Rubahn, H.-G.; Bergmann, K. *Annu. Rev. Phys. Chem.* **1990**, *41*, 735–773.
- (21) Krajnovich, D. J.; Butz, K. W.; Du, H.; Parmenter, C. S. *J. Chem. Phys.* **1989**, *91*, 7725–7739.
- (22) Ziegler, G.; Kumar, S. V. K.; Rubahn, H.-G.; Kuhn, A.; Sun, B.; Bergmann, K. *J. Chem. Phys.* **1991**, *94*, 4252–4259.
- (23) Alexander, M. H.; Berning, A.; Degli Esposti, A.; Jörg, A.; Kliesch, A.; Werner, H.-J. *Ber. Bunsen-Ges. Phys. Chem.* **1990**, *94*, 1253–1262.
- (24) Alexander, M. H.; Werner, H.-J. *J. Chem. Phys.* **1991**, *95*, 6524–6535.
- (25) Billeb, A.; Stewart, B. *Chem. Phys. Lett.* **1995**, *247*, 433–439.
- (26) Franck, J.; Wood, R. W. *Philos. Mag.* **1911**, *21*, 314–318.
- (27) Gao, Y.; Gorgone, P. S.; Davis, S.; McCall, E. K.; Stewart, B. *J. Chem. Phys.* **1996**, *104*, 1415–1426.
- (28) Baumgartner, G.; Kornmeier, H.; Preuss, W. *Chem. Phys. Lett.* **1984**, *107*, 13–21.
- (29) Schmidt-Minck, I.; Müller, W.; Meyer, W. *Chem. Phys.* **1985**, *92*, 263–285.
- (30) Nesmeyanov, A. N. *Vapor Pressure of the Chemical Elements*; Academic Press: New York, 1963.

- (31) Kusch, P.; Hessel, M. M. *J. Chem. Phys.* **1977**, *67*, 586–589.
- (32) Zare, R. N. *Angular Momentum*; Wiley-Interscience: New York, 1988.
- (33) Barakat, B.; Bacis, R.; Carrot, F.; Churassy, S.; Crozet, P.; Martin, F.; Verges, J. *Chem. Phys.* **1986**, *102*, 215–227.
- (34) Ratcliff, L. B.; Fish, J. L.; Konowalow, D. D. *J. Mol. Spectrosc.* **1987**, *122*, 293–312.
- (35) Preuss, W.; Baumgartner, G. Z. *Phys. A* **1985**, *320*, 125–133.
- (36) Derouard, J.; Sadeghi, N. *Chem. Phys. Lett.* **1984**, *111*, 353–359.
- (37) McGuire, P.; Kouri, D. J. *J. Chem. Phys.* **1974**, *60*, 2488–2499.
- (38) McGuire, P. *J. Chem. Phys.* **1975**, *62*, 525–534.
- (39) Gao, Y.; Stewart, B. J. *Chem. Phys.* **1995**, *103*, 860–863.
- (40) Cooper, L. K.; McCaffery, A. J.; Bosanac, S. D. *Chem. Phys. Lett.* **1990**, *167*, 233–238.
- (41) Smith, N. J. *Chem. Phys.* **1986**, *85*, 1987–1995.
- (42) Pattengill, M. D. Rotational Excitation III: Classical Trajectory Methods. In *Atom-Molecule Collision Theory: A Guide for the Experimentalist*; Bernstein, R. B., Ed.; Plenum: New York, 1979.
- (43) Gentry, W. R. Vibrational Excitation II: Classical and Semiclassical Methods. In *Atom-Molecule Collision Theory: A Guide for the Experimentalist*; Bernstein, R. B., Ed.; Plenum: New York, 1979.
- (44) McBane, G. C. “PMP Molscat”, a parallel version of Molscat version 14; Grand Valley State University, 2005. available at <http://faculty.gvsu.edu/mcbaneg/pmpmolscat>.
- (45) Hutson, J. M.; Green, S. *MOLSCAT computer code, version 14*, distributed by Collaborative Computational Project No. 6 of the Engineering and Physical Sciences Research Council (U.K.), 1994.
- (46) Urbanski, K.; Antonova, S.; Yiannopoulou, A.; Lyyra, A. M.; Li, L.; Stwalley, W. C. *J. Chem. Phys.* **1996**, *104*, 2813–2817.
- (47) Urbanski, K.; Antonova, S.; Yiannopoulou, A.; Lyyra, A. M.; Li, L.; Stwalley, W. C. *J. Chem. Phys.* **2002**, *116*, 10557–10557.
- (48) LeRoy, R. J. *LEVEL 8.0: A Computer Program for Solving the Radial Schrodinger Equation for Bound and Quasibound Levels*, University of Waterloo Chemical Physics Research Report CP-663 (2007); see <http://leroy.uwaterloo.ca/programs/>.
- (49) Manolopoulos, D. E. *J. Chem. Phys.* **1986**, *85*, 6425–6429.
- (50) Alexander, M. H.; Manolopoulos, D. E. *J. Chem. Phys.* **1987**, *86*, 2044–2050.
- (51) Smith, N.; Scott, T. P.; Pritchard, D. E. *J. Chem. Phys.* **1984**, *81*, 1229–1247.
- (52) Stewart, B. *Chem. Phys. Lett.* **1995**, *245*, 643–647.
- (53) DePristo, A. E.; Augustin, S. D.; Ramaswamy, R.; Rabitz, H. *J. Chem. Phys.* **1979**, *71*, 850–865.
- (54) Brunner, T. A.; Pritchard, D. Fitting Laws for Rotationally Inelastic Collisions. In *Advances in Chemical Physics: Dynamics of the Excited State, Vol. 50*; Lawley, K. P., Ed.; John Wiley and Sons, Ltd.: New York, 1982.
- (55) Scott, T. P.; Smith, N.; Pritchard, D. E. *J. Chem. Phys.* **1984**, *80*, 4841–4850.
- (56) Note that the adiabatic factor *A* is squared in eq 9. There is a typographical error in ref 27.
- (57) Brunner, T. A.; Scott, T. P.; Pritchard, D. E. *J. Chem. Phys.* **1982**, *76*, 5641–5643.
- (58) Dexheimer, S. L.; Durand, M.; Brunner, T. A.; Pritchard, D. E. *J. Chem. Phys.* **1982**, *76*, 4996–5004.
- (59) Brian Stewart and George C. McBane, manuscript in preparation.
- (60) Massey, H. S. W. *Rep. Prog. Phys.* **1949**, *12*, 248–269.
- (61) Born, M.; Mayer, J. E. Z. *Phys.* **1932**, *75*, 1–18.
- (62) Peterson, K. A. Private communication.

JP103504A